ACS APPLIED MATERIALS & INTERFACES

www.acsami.org

Research Article

Enhanced Electromagnetic Shielding and Thermal Management Properties in MXene/Aramid Nanofiber Films Fabricated by Intermittent Filtration

Chenxu Liu, Yanan Ma, Yimei Xie, Junjie Zou, Han Wu, Shaohui Peng, Wei Qian, Daping He, Xin Zhang, Bao-Wen Li,* and Ce-Wen Nan

Cite This: *ACS Appl. Mater. Interfaces* 2023, 15, 4516−4526

Read Online

ACCESS | Metrics & More | Article Recommendations | Supporting Information

ABSTRACT: High-efficiency electromagnetic interference (EMI) shielding and heat dissipation synergy materials with flexible, robust, and environmental stability are urgently demanded in next-generation integration electronic devices. In this work, we report the lamellar MXene/Aramid nanofiber (ANF) composite films, which establish a nacre-like structure for EMI shielding and heat dissipation by using the intermittent filtration strategy. The MXene/ANF composite film filled with 50 wt % MXene demonstrates enhanced mechanical properties with a strength of 230.5 MPa, an elongation at break of 6.2%, and a toughness of 11.8 MJ·m^3 (50 wt % MXene). These remarkable properties are attributed to the hydrogen bonding and highly oriented structure. Furthermore, due to the formation of the MXene conductive network, the MXene/ANF composite film shows an outstanding conductivity of 624.6 S/cm, an EMI shielding effectiveness (EMI SE) of 44.0 dB, and a superior specific SE value (SSE/t) of 18847.6 dB·cm^2/g, which is better than the vacuum filtration film. Moreover, the MXene/ANF composite film also shows a great thermal conductivity of 0.43 W/m·K. The multifunctional MXene/ANF composite films with high-performance EMI shielding, heat dissipation, and joule heating show great potential in the field of aerospace, military, microelectronics, microcircuit, and smart wearable electronics.

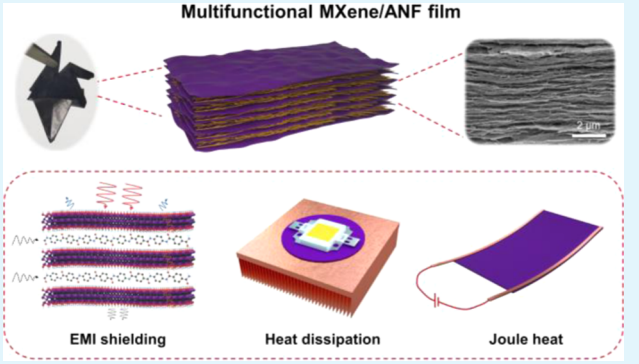

KEYWORDS: *MXene nanosheets, Aramid nanofiber, mechanical properties, electromagnetic interference shielding (EMI), thermal management*

1. INTRODUCTION

5G communication technology has promoted the booming development of smart wearable electronic devices. Accompanied by high integration and increases in power density, the electronic device will not only generate plenty of electromagnetic waves in different frequency bands but also cause thermal management issues.[1−4] These problems severely restrict the working accuracy and stability of systems, which destroys the body's health and increases the risk of diseases. Therefore, it is critical to develop and integrate electromagnetic interference (EMI) and heat dissipation materials with high performance for next-generation wearable electronics.

In general, polymer composites with conductive fillers (such as graphene,[5−9] carbon nanotubes,[10−13] metal nanoparticles and nanowires[14,15]) have been widely explored in terms of flexible EMI shielding and thermal management films owing to their favorable lightweight, anticorrosion, and machinability.[16−21] Nevertheless, most fillers are short of functional groups, which are difficult to disperse uniformly in the matrix. On the other hand, the EMI shielding and thermal management performance should be further enhanced simultaneously to satisfy commercial requirements. So, seeking the appropriate fillers and improving their distribution and orientation in the matrix can greatly improve the electromagnetic shielding and heat conduction of polymer composites while maintaining desirable mechanical properties.[22−24]

MXene has been widely applied in the fields of EMI shielding due to its superior metallic conductivity, lightweight, large specific surface area, and ease of processing.[25−31] For example, a free-standing $Ti_3C_2T_x$ film exhibited a distinguished electrical conductivity and EMI shielding effectiveness (EMI SE) of 4665.1 S/cm and 92 dB, respectively.[32] However,

Received: November 8, 2022
Accepted: January 4, 2023
Published: January 13, 2023

oxidation and self-stacking often tend to happen in a pure MXene film during the applied process, which deteriorates the mechanical properties. It has been reported that introducing 1D nanomaterials into MXene films can compensate and improve their robustness.[33] For example, Cao et al. have designed the $Ti_3C_2T_x$/CNF/CNF film, achieving a mechanical strength of 135.4 MPa and EMI shielding efficiency of 2647 dB·cm^2/g.[34] Notably, 1D Aramid nanofiber (ANF) has been regarded as the most promising reinforcement in composite materials due to its superior mechanical properties, good chemical resistance, and flame retardancy.[35−37] In addition, ANF displays rich functional groups, which is conducive to forming strong interactions with MXene through the valence bond effect.[38,39] 1D ANF and 2D MXene nanosheets can form lamellar structure to simultaneously enhance the mechanical and thermal performance of the materials.[40,41] However, the common preparation methods of MXene-based composites are hard to tune the orientation and distribution of the fillers, which enormously leads to the aggregation of nanosheets. Thus, it remains a challenge to balance the electrical conductivity, mechanical strength, and thermal management of the composite films by increasing the orientation of MXene.[42−45]

Herein, flexible, super-strength, and highly oriented MXene/ANF composite films with the "brick−mortar" structure were fabricated by intermittent filtration for EMI shielding and heat dissipation applications. The MXene/ANF composite film displayed an outstanding mechanical strength of 230.5 MPa, an elongation at break of 6.2%, and a toughness of 11.8 MJ/m^3 due to the synergistic effect between the 1D rigid rodlike ANF and 2D MXene. More importantly, the MXene nanosheets have highly oriented distribution in the matrix to form electrically conductive paths, resulting in a high conductivity of 624.6 S/cm and an EMI shielding efficiency of 44.0 dB. The MXene/ANF composite films also exhibited remarkable heat dissipation capacity and stable Joule heating performance, which is applied for thermal interface material to cool LED chips.

2. EXPERIMENTAL SECTION

2.1. Chemicals and Materials. The *p*-phenylene terephthalamide (PPTA) yarns were purchased from Yantai Tayho Advanced Materials Co., Ltd. MAX precursor (Ti_3AlC_2, ≥99.99%, 200 mesh) powder was purchased from Jilin 11 Technology Co., Ltd. Lithium fluoride (LiF, ≥99.995%, AR) was provided by Sigma-Aldrich Co. Ltd. Dimethyl sulfoxide (DMSO, ≥99.8%, AR) was supplied by the Aladdin Reagent Co. Ltd. Potassium hydroxide (KOH, AR) and hydrochloric acid (HCl, 36.0−38.0 wt % in H_2O) were supplied by Sinopharm Chemical Reagent Co., Ltd.

2.2. Preparation of the ANF Dispersion. The ANF dispersion was synthesized from PPTA yarns based on the proton donor-assisted deprotonation method.[46] In detail, 0.3 g of PPTA yarns, 0.45 g of KOH, and 6 mL of DI water were first added to 150 mL of DMSO in sequence. The mixed solution was magnetically stirred for 6 h at room temperature. Then, the above ANF/DMSO solution was added to 300 mL of DI water with magnetic stirring for 30 min. The mixture solution was repeatedly washed with alcohol and deionized water to eliminate the redundant KOH and DMSO. Finally, 0.3 g of ANF was dispersed in 600 mL of DI water under mechanical stirring, and a homogeneous ANF/water dispersion was acquired.

2.3. Synthesis of $Ti_3C_2T_X$. $Ti_3C_2T_x$ was exfoliated by a minimally intensive layer delamination (MILD) method.[47,48] First, 3 g of LiF was added to 40 mL of 9 M HCl solution in a Teflon vessel and continuously stirred for 30 min. Next, 2 g of Ti_3AlC_2 powder was slowly poured into the etching solution by constantly stirring for 48 h at 35°C. After etching, the reaction mixture was washed with DI water and centrifuged to remove the HCl and LiF. Subsequently, the supernatant was ultrasonically stratified for 30 min under an Ar flow. Finally, the MXene aqueous dispersion was prepared by centrifuging for 30 min to remove the unexfoliated powder.

2.4. Preparation of the MXene/ANF Composite Films. The ANF dispersion was uniformly mixed with MXene dispersion and sonicated for 10 min. Subsequently, the mixture was added into the sand core funnel several times using intermittent filtration. A series of films were prepared by intermittent filtration and dried in the oven for 13 h. The MXene/ANF composite films were hot-pressed at 60°C for 30 min. For comparison, the mixtures containing ANF films and MXene were added into the sand core at one time using the vacuum filtration strategy. For brevity, MXene/ANF composite films are marked as MA−X%, where X represents the MXene content.

2.5. Characterization of Materials. The microstructures of $Ti_3C_2T_x$ MXene, ANF, and MXene/ANF were collected using a scanning electron microscope (SEM, Zeiss Ultra Plus) and a field emission transmission electron microscope (TEM, Talos F200S). The thickness and morphological structures of MXene were examined by atomic force microscopy (AFM, Cypher ES). The crystalline structures of the powder and film samples were determined by X-ray diffraction (XRD, Rigaku Smartlab). Small-angle X-ray scattering (SAXS) was conducted on a NanoSTAR SAXS system (Bruker-AXS). The elemental compositions and chemical bonds of $Ti_3C_2T_x$ MXene, ANF, and MXene/ANF were measured by X-ray photoelectron spectroscopy (XPS, ESCALAB 250Xi). Fourier transform infrared (FTIR) spectra of the above films were performed using an FTIR spectrometer (Nicolet6700).

The mechanical properties of the MXene/ANF composite film were recorded by an electronic universal testing machine (MTS Criterion44). The samples for the tensile test were cut into regular strips, the sample width and gauge length for all of the films were 3 and 10 mm, and the loading rate was 1 mm/min. The sheet resistance was collected by a four-point probe instrument (RTS-9).

2.5.1. EMI Property Characterization of MXene/ANF Composite Films. The EMI SE of composite films was collected using a vector network analyzer (PNA Network Analyzer, N5244B) in the frequency ranging from 8.2 to 12.4 GHz (X-band) at an ambient temperature. The S_{11} and S_{21} were measured to evaluate the coefficients of transmission (T), reflection (R), and absorption (A) coefficients.

The total electromagnetic shielding effectiveness (SE_T), microwave absorption (SE_A), and microwave reflection (SE_R) were calculated from the following formulas

$$R = |S_{11}|^2$$

$$T = |S_{21}|^2$$

$$A = 1 - R - T$$

$$SE_R = -10\log(1 - R) = -10\log(1 - |S_{11}|^2)$$

$$SE_A = -10\log\left(\frac{T}{1 - T}\right) = -10\log\left(\frac{|S_{21}|^2}{1 - |S_{11}|^2}\right)$$

$$SE_T = SE_R + SE_A + SE_M$$

When the SE_T is over 15 dB, the SE_M can be ignored. The specific SE value (SSE/t) is used to evaluate the effectiveness of the shielding material to eliminate the effects of density and thickness

$$SSE/t = \frac{\text{EMI SE}}{\text{density} \times \text{thickness}} = \text{dB cm}^2/\text{g}$$

2.5.2. Thermal Property Characterization of MXene/ANF Composite Films. The thermal conductivity of MXene/ANF composite films was calculated by the following equation

$$\lambda = \alpha \times C_p \times \rho$$

https://doi.org/10.1021/acsami.2c20101
ACS Appl. Mater. Interfaces 2023, 15, 4516−4526

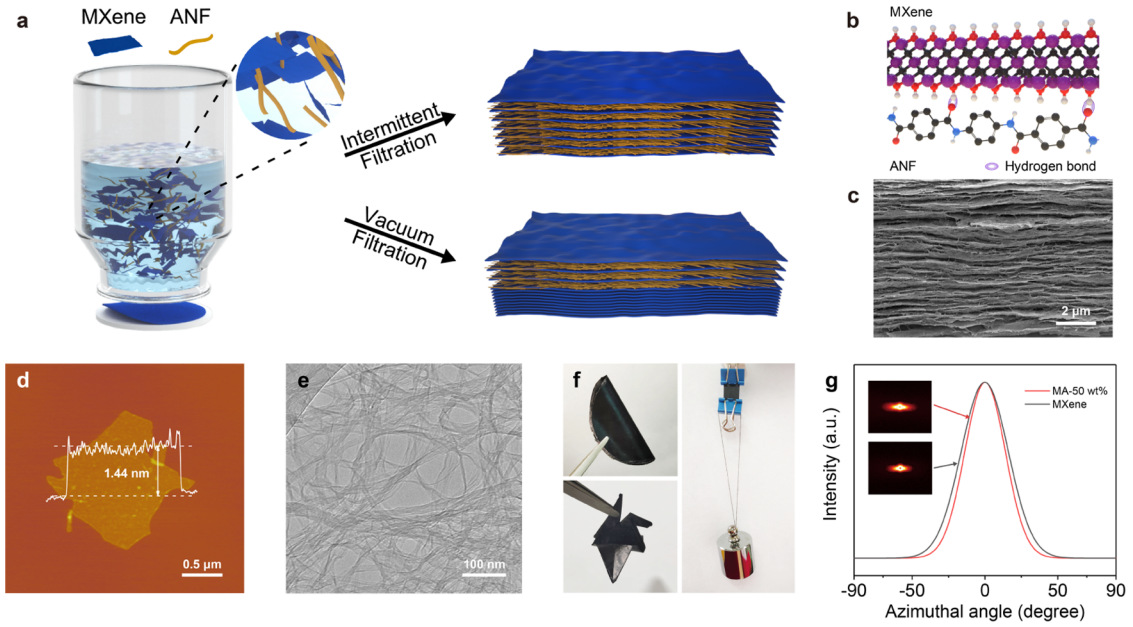

Figure 1. (a) Schematic illustration showing the fabrication of the MXene/ANF films. (b) Schematic illustration of the ball-and-stick model of the MXene/ANF film. (c) Cross-sectional SEM image of the MXene/ANF film. (d) AFM image of an individual MXene. (e) TEM images of ANF. (f) Optical photographs of the MXene/ANF film. (g) 2D SAXS azimuthal angle plots of the MXene/ANF and MXene films.

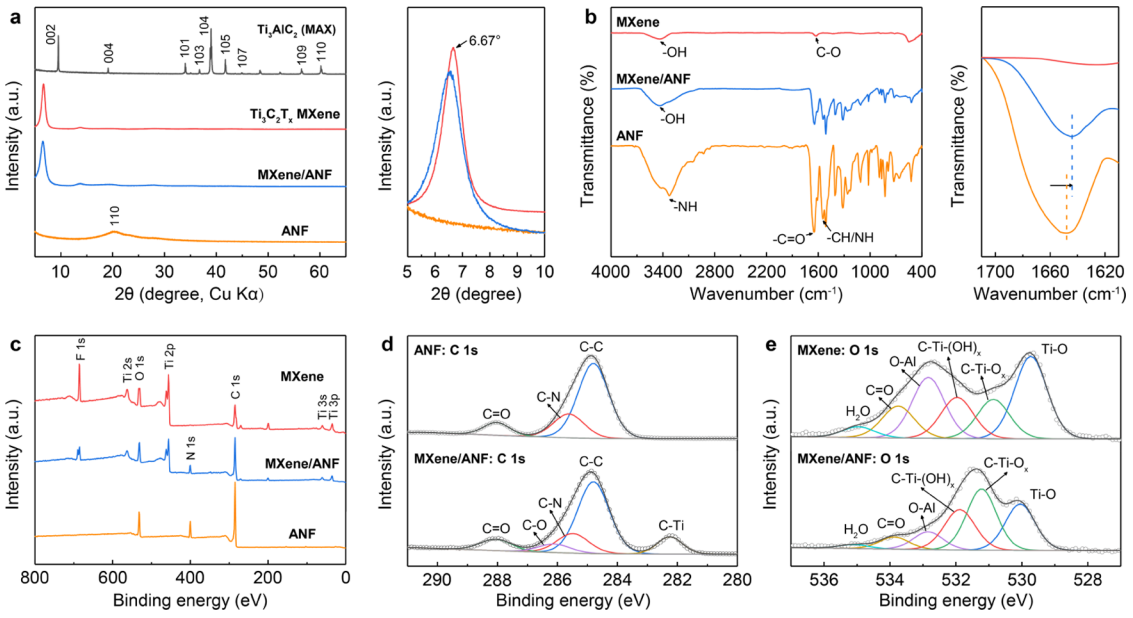

Figure 2. (a) XRD patterns of Ti_3AlC_2 (MAX), MXene, ANF, and MXene/ANF films. (b) FTIR spectra of ANF, MXene, and MXene/ANF films. (c) XPS spectra of MXene, ANF, and MXene/ANF films. (d) High-resolution XPS spectra of C 1s for ANF and MXene/ANF films. (e) High-resolution XPS spectra of O 1s for MXene and MXene/ANF films.

where the λ, α, C_p, and ρ represented the thermal conductivity, thermal diffusivity, heat capacity, and density, respectively. The thermal diffusivity of films was recorded by the laser flash method (LFA 467 NanoFlash, Netzsch). The heat capacity was measured by a differential scanning calorimeter (DSC 8500, PerkinElmer). The thermal images of the surface temperature were collected by an infrared thermal imager (HIKMICRO). A constant voltage was supplied by a DC Power Supply (Rigol, DP832).

3. RESULTS AND DISCUSSION

3.1. Morphological Characteristics of MXene/ANF Composite Films. The schematic for fabricating flexible and robust MXene/ANF composite films is shown in Figure 1a. MXene nanosheets were first synthesized by selectively etching Al layers from MAX (Figure S1a) using LiF/HCl mixed solution. AFM and TEM images revealed the ultrathin and transparent MXene with a thickness of 1.44 nm, indicative of its successful exfoliation (Figures 1d and S1b). Then, the 1D rigid rodlike ANF was prepared via the proton donor-assisted deprotonation process (Figure 1e) in the KOH/DMSO system. In the deprotonation process, KOH/DMSO permeates into the inside of the pristine PPTA, weakening the hydrogen bonding and extracting the mobile hydrogen from the amide groups. A small number of proton donors decrease the viscosity of the ANF/DMSO dispersion and increase the

https://doi.org/10.1021/acsami.2c20101
ACS Appl. Mater. Interfaces 2023, 15, 4516−4526

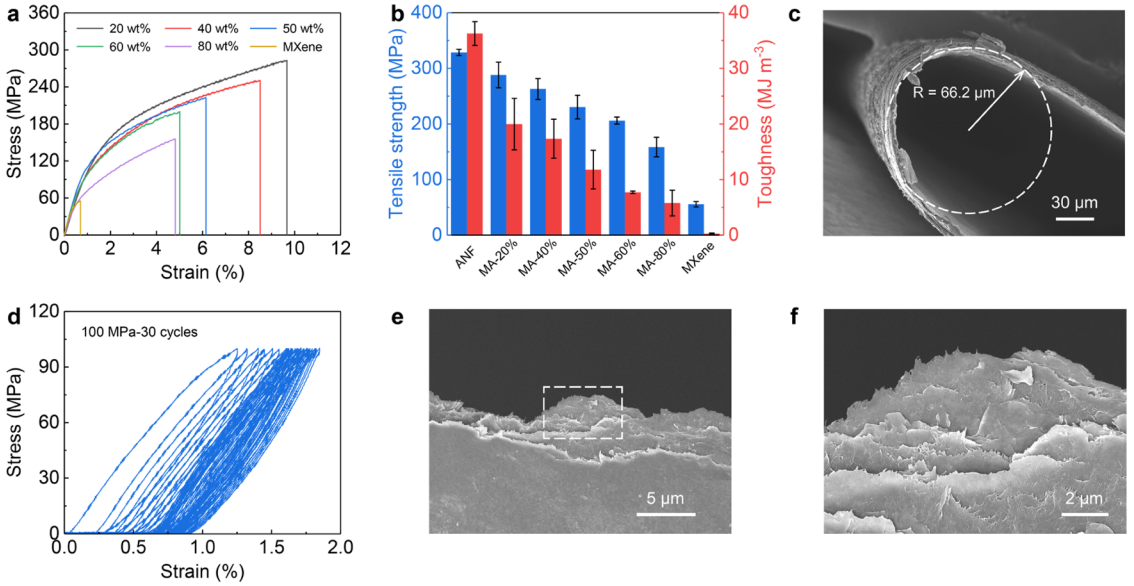

Figure 3. (a) Stress−strain curves and (b) tensile strength and toughness of MXene/ANF films with different MXene contents. (c) Cross-sectional SEM image of the bending MXene/ANF film. (d) Stress−strain curves with a constant stress of 100 MPa for 30 cycles. (e) and (f) SEM images of the fracture surface.

degree of deprotonation.[49] Subsequently, a highly stable and homogeneous ANF/DMSO dispersion was obtained, owing to the $\pi-\pi$ stacking, electrostatic repulsion, and hydrophobic attraction between ANF materials (Figure S2). Moreover, an obvious Tyndall effect was observed in all aqueous dispersions of ANF, MXene, and MXene/ANF, verifying the stable and well-exfoliated colloidal characteristics (Figure S3).

The MXene/ANF composite films were assembled by the intermittent filtration technique and then hot-pressing treatment (Figure S4). Especially, the mixture containing MXene and ANF was divided into multiple stages during the filtration process, thus improving the homogeneity and specific area of films, which is different from the conventional filtration strategy. The cross-sectional SEM and energy-dispersive spectrometer elemental maps of the MXene/ANF verify the filler dispersion of the two strategies (Figure S5). By conventional vacuum filtration, a large amount of MXene is deposited at the bottom of the film and displays a dense stack, which can be verified by the inconsistent conductivity on both sides of the resulting composite films (Figure S6). On the contrary, the film via intermittent filtration shows a uniform lamellar structure. As shown in Figures 1b,c and S7−S9, MXene nanosheets are tightly interacted with hydrogen bonding by the ANF to form the "brick−mortar" structure, as revealed by SEM images of MXene and MXene/ANF composite films. Figure 1f shows that the MXene/ANF composite film can be folded into a complex model or loaded with a weight of 200 g, demonstrating the superior mechanical performance. The SAXS was further used to quantify the alignment degree of nanosheets. The MXene/ANF composite film exhibits narrower peaks and a higher Herman orientation factor (f = 0.85) compared to the pristine MXene film. Therefore, the interaction between ANF and MXene can enhance the orientation and stacking of the MXene/ANF composite films (Figure 1g).

Figure 2a shows the XRD patterns of MAX, MXene, ANF, and MXene/ANF composite films. Compared with the Ti_3AlC_2 powder, the characteristic peak (002) of MXene shifts from 9.5 to 6.7°, and other characteristic peaks of MAX such as (101), (103), (104), (105), and (107) disappear after the ultrasonication process, further proving the successful synthesis of MXene. Only diffraction peaks arising from the (002) and (004) planes of MXene and the (110) plane of ANF are observed in the XRD pattern of composite film, verifying the good interaction of MXene and ANF. It is worth noting that the characteristic peak (002) of MXene/ANF shifts to a lower angle, which indicates that the ANF is successfully added to the MXene layers.

FTIR spectra and XPS were also used to analyze the valence bond and the chemical structure of the ANF, MXene, and MXene/ANF composite films. The absorption peaks are located at 3427 and 1630 cm^{-1} appearing in the FTIR spectrum of MXene, which can be ascribed to the vibration of the hydroxyl (-OH) and C−O (Figure 2b). In addition, the peaks are located at 3325 and 1544 cm^{-1} in the FTIR spectrum of ANF, corresponding to the stretching vibration and deformation of N−H, respectively, while the peak at 1646 cm^{-1} to the stretching vibration of C═O. The most characteristic peaks of MXene and ANF are all observed in the MXene/ANF composite film. However, some subtle differences appear in the film. For example, the characteristic peak of −OH at 1648 cm^{-1} for the ANF shifts red to 1644 cm^{-1} in the MXene/ANF composite film, proving the hydrogen bonding between ANF and MXene during the self-assembly preparation process.[39] The vibrational absorption peak of −OH for MXene/ANF is lower than that for MXene, which also confirmed the effect of hydrogen bonding.

The XPS spectra of the MXene, ANF, and MXene/ANF composite films and the component peaking-fitting for C 1s and O 1s are shown in Figures 2c−e and S10. Clearly, the terminal groups incorporating fluorine (−F), oxide (−O), and hydroxyl (−OH) appear in the XPS spectrum of MXene, suggesting that abundant functional groups are introduced to the surface and edge during the material synthesis processes. After the introduction of ANF, the main peaks of MXene and ANF arise simultaneously in the relevant XPS spectra.

https://doi.org/10.1021/acsami.2c20101
ACS Appl. Mater. Interfaces 2023, 15, 4516−4526

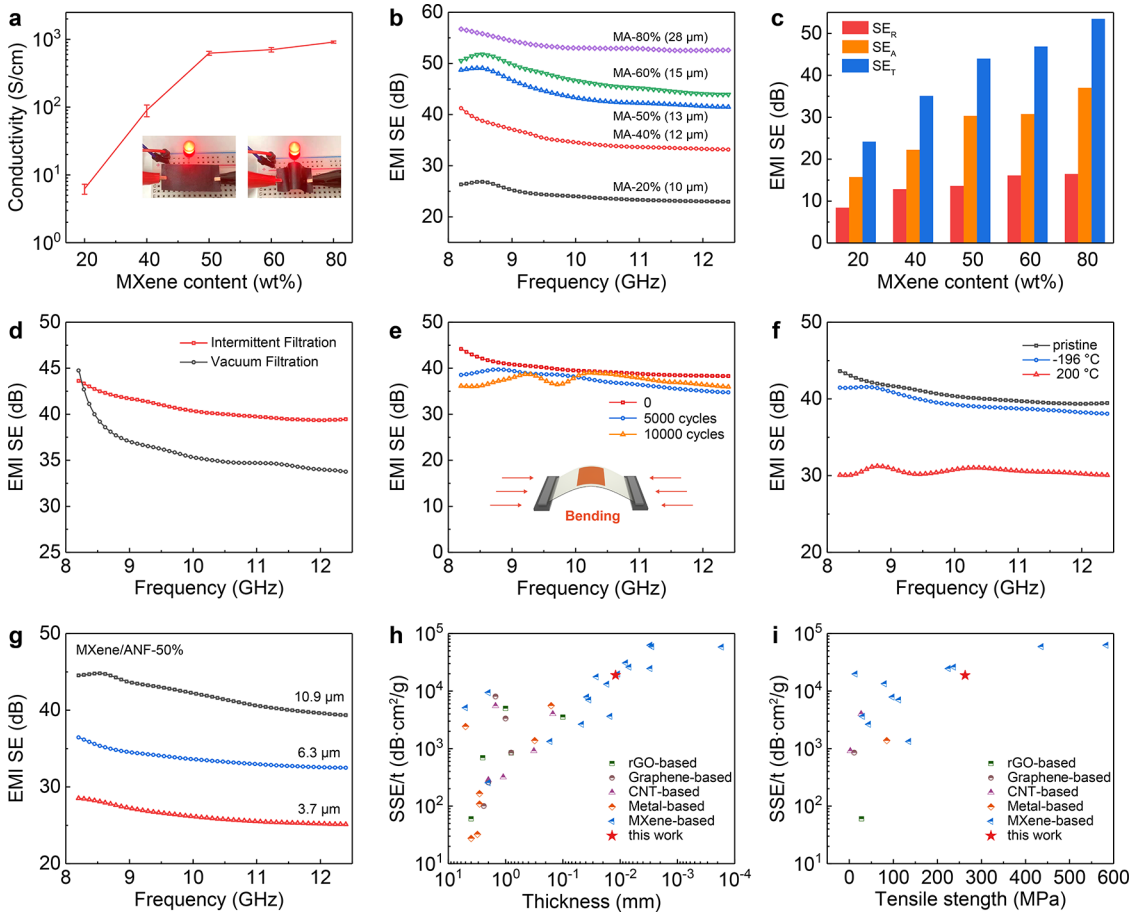

Figure 4. (a) Electrical conductivity plotted as a function of the MXene content. (b) EMI SE in the X-band (8.2−12.4 GHz). (c) Comparison of SE_T, SE_A, and SE_R of the MXene/ANF films with different MXene contents. (d) EMI SE of the MXene/ANF films with different preparation strategies. (e) EMI SE of the MXene/ANF films with different bending cycles. (f) EMI SE of MXene/ANF films after heating or cooling at different temperatures. (g) EMI SE of the MXene/ANF films with different thicknesses in the X-band. Comparison of the MXene/ANF films with other reported materials of SSE/t and (h) thickness and (i) tensile strength.

Compared with ANF, the C 1s spectra of MXene/ANF exhibit a new C−N peak at 285.5 eV and C−Ti peak at 282.3 eV, demonstrating the successful integration of ANF and MXene into the composite film. As shown in Figure 2e, the characteristic peaks appearing at 530.1, 531.2, 531.9, 532.8, 533.9, and 535.1 eV represent the Ti−O, C−Ti−O_x, C−Ti−$(OH)_x$, O−Al, and C═O and adsorb water in the MXene/ANF composite film, respectively. Besides, the characteristic peak of the C−Ti−$(OH)_x$ bond located at 521.9 eV for MXene changes to 532.0 eV for MXene/ANF, and a new peak appears at 286.2 eV in the C 1s XPS spectra, which corresponds to the C−O bond. This result suggests that the chemical environment and hydrogen bond have been changed during the preparation.

3.2. Mechanical Characteristics of MXene/ANF Composite Films. Additionally, high-performance EMI shielding materials require excellent mechanical strength and adequate flexibility for complex applications. Typically, the self-assembled MXene films possess poor mechanical properties and weak oxidation resistance, which hinder the mass production for applications. After integration with ANF, remarkable mechanical improvement including the tensile strength, elongation at break, and toughness of the composite films is revealed by the tensile stress−strain curves of the MXene/ANF composite films (Figures 3a and S11). Especially, the MA-80% exhibits a strength of 155.7 MPa, an elongation at break of 4.8%, and a toughness of 5.8 MJ/m^3, which are 2.85, 4.8, and 21.1 times than those of pure MXene films, respectively. (Table S2). With the increase of the ANF content, the mechanical performances of MXene/ANF composite films continuously increase and finally achieve an optimum tensile strength of 282.5 MPa, an elongation at break of 9.7%, and a toughness of 20.0 MJ/m^3 at the MA-20% (Figure 3b).

The hydrogen bonding of 1D ANF and 2D MXene nanosheets and the building "brick−mortar" structure is essential to achieve a tough, flexible, and robust mechanical strength. To substantiate the reliability and stability of MXene/ANF, the cyclic tensile tests were carried out in EMI shielding materials. Figure 3c shows the SEM image of the MXene/ANF film bent at 180°; the film remains in a compact structure, indicating that it has sufficient flexibility and mechanical strength. As shown in Figure 3d, the cyclic tensile load of MXene/ANF film was recorded under a constant pretension stress of 100 MPa. While the stress−strain curves prove irreversible deformation of the MXene/ANF structure during stretching, the strain degree slightly changes and the film still exhibits good fatigue resistance during deformation. Besides, the surface morphology of MXene/ANF films was evaluated to understand the fracture mechanism (Figures 3e−f and S12). At

https://doi.org/10.1021/acsami.2c20101
ACS Appl. Mater. Interfaces 2023, 15, 4516−4526

the initial stage of stretching, the tensile stress straightens the curved ANF chains and the wrinkled MXene nanosheets, while the entirety structure of the MXene/ANF film remains intact. With further stress loading, MXene slips relatively and gradually breaks to form stepped cracks. The curly fracture edges and multistep cracking path appear in the magnified region of the surface of the MXene/ANF composite film. The cracking path growth can absorb an amount of fracture energy, which was ascribed to the hydrogen bonding and interface interactions between the ANF and MXene.[44,50] Moreover, partial fibers are pulled out along the stretching direction, and therefore, the stress will be effectively passed from MXene nanosheets to the ANF internetwork during the cracking path growth, resulting in remarkable mechanical reinforcement.[51] Figure S13 shows the photographs of the films under different ultrasonication times. While the pure MXene film starts to dissolve into powder after ultrasonication for 0.5 min, whereas the composite film exhibits superb stability after ultrasonication for 10 min. In addition, the contact angle of the MXene film is 51.4°, which is improved to be 61.6° after integration with ANF. These results suggest the improved resistance to harsh conditions in the MXene/ANF composite film (Figure S14).

3.3. Electrical and EMI Shielding Performances of MXene/ANF Composite Films. Figure 4a shows the conductivity of the MXene/ANF composite films with different ratios. In terms of percolation theory, increasing contact areas and conductive paths will be established in the MXene/ANF composite films with the MXene content increasing from 20 to 50 wt %, resulting in significantly increased electrical conductivity in the resulting composite film. However, the electrical conductivity nearly remains unchanged above 50 wt % MXene content. A high electrical conductivity of up to 913.4 ± 32.8 S/cm is realized at the maximum content of MA-80%. As demonstrated in the insets of Figure 4a, the brightness of the LED light remains unchanged after bending and stretching, indicating its excellent flexibility and electrical conductivity. Figure 4b shows the EMI SE of the MXene/ANF composite films in the frequency ranging from 8.2 to 12.4 GHz. The SE_T increases rapidly with the increase of content, which stays with the continuous increase in electrical conductivity of the composite film. With a low content of MA-20%, the composite film presents a relatively high EMI SE of 24.1 dB, which can satisfy the demands of EMI shielding applications (higher than 20 dB). When the content of MXene increases up to 80 wt %, the EMI SE increases to 53.5 dB because of the more remarkable electric conductivity. Besides, the theoretical EMI SE is calculated by the Simon equation

$$SE = 50 + 10 \log \frac{\sigma}{f} + 1.7t\sqrt{\sigma f}$$

where σ, f, and t are the electrical conductivity, frequency, and thickness of films, respectively.[52] The calculated EMI SE values are consistent with the experimental results (Figure S15). As shown in Figure 4c, the SE_T, SE_A, and SE_R values are measured to analyze the mechanism of EMI shielding. With the MXene content enhanced, the SE_A values of MXene/ANF exhibit a greater increasing trend than SE_R. This result proves that microwave absorption, rather than reflection, is the dominant shielding mechanism. Furthermore, the MXene/ANF composite films represent extremely high shielding efficiency above 99.9% (Figure S16 and Table S1).

The performance of MXene/ANF composite films is processed by two strategies, as shown in Figure 4d. The EMI SE of the intermittent filtration film is obviously better than that of the vacuum filtration film, confirming that the uniform structure facilitates the loss of electromagnetic wave. To verify the adaptive capacity of the MXene/ANF composite films for various complex deformations, the bending resistances of two types of films are tested (Figure S17a,b). Due to the introduction of the rigid ANF, the EMI efficiency of the two strategy films remains above 98% after bending 5000 cycles, and the electrical conductivity of the intermittent filtration film remains basically unchanged in the meantime. Figures 4e and S17c show the EMI SE and electrical stability of the MA-50 wt % film during bending and stretching 10 000 cycles, respectively. The bend radius and stretch distance were controlled by a computer-controlled stepping motor. The EMI SE value decreases from 38.5 to 35.8 dB after bending 10 000 cycles, with a 93.0% electromagnetic shielding performance retention. The MXene/ANF composite films present steady electrical signals under repeated bending and stretching states at a fixed frequency of 2 Hz (Figure S17c). After bending 10 000 cycles, a dense structure is almost kept in the composite film, without obvious cracks and holes in the film surface (Figure S18). The excellent electrical stability and bending durability are enabled by the "brick-mortar" structure and hydrogen-bonding interaction between ANF and MXene. We also verify the potential application of MXene/ANF composite films under extreme temperature environments, as shown in Figure 4f. The EMI shielding efficiency only exhibits a slight decrease in liquid nitrogen for 0.5 h or heating at 200 °C for 0.5 h in air, confirming that the ANF restrains the destruction of the MXene structure.

The thickness and the density of the composites are crucial factors that influence the EMI shielding performance in practical applications. Thus, the EMI shielding performances of MA-50% with different thicknesses were measured. As expected, EMI SE monotonically increases with the increase of thickness (Figure 4g). To avoid the influence of density and thickness in the diverse system, SSE/t is introduced to evaluate the EMI shielding property of the film. The maximum value of SSE/t achieve is 18 847.6 dB·cm^2/g with the 50 wt % MXene content, as shown in Table S3. The MXene/ANF composite films possess excellent EMI shielding performance according to the relationship between the thickness and SSE/t of films (Figure 4h–i), which is better than that of other materials. To discuss the EMI shielding mechanism, a detailed drawing is described in Figure S19, which displays the interaction process of the electromagnetic waves and the MXene/ANF composite material. When the electromagnetic waves come onto the surface of the composite film, the portion of the electromagnetic waves is reflected directly at the interface because of the impedance mismatch between the air and the composite film. Subsequently, the residual electromagnetic waves further pass into the interior of the film, interact with the high-density electron of the MXene, and generate induced currents, leading to the partial absorption of the electromagnetic wave. In addition, the multistage internal reflections of the neighboring MXene facilitate the loss of partial electromagnetic waves.[53] The synergistic effect of multiple shielding actions endows the remarkable EMI shielding property of the composite films.

3.4. Thermal Management Performances of MXene/ANF Composite Films. The MXene/ANF composite films also present a huge potential for thermal management. Figure

https://doi.org/10.1021/acsami.2c20101
ACS Appl. Mater. Interfaces 2023, 15, 4516–4526

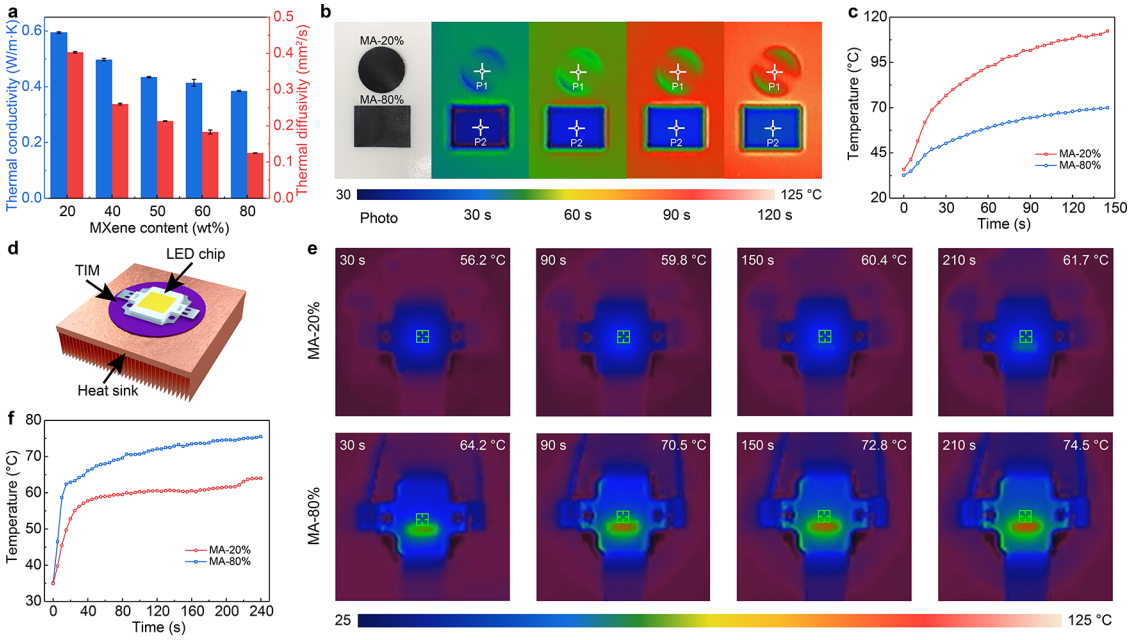

Figure 5. (a) Through-plane thermal conductivity and diffusivity of the MXene/ANF films. (b) Infrared thermal images and (c) surface temperature evolution of MA-20% and MA-80% after continuous heating. (d) Schematic diagram of the system configuration for LED cooling. (e) Infrared thermal images of the LED chip with different TIM and (f) the corresponding time-dependent temperature curves.

5a exhibits the through-plane thermal conductivity and thermal diffusivity of the MXene/ANF composite films. The thermal conductivity of the composite films clearly increases with the content of ANF, and the highest thermal conductivity and thermal diffusivity reach 0.59 W/m·K and 0.4 mm^2/s in the MA-20%, respectively. The thermal conductive pathways are formed by the interconnected ANF frameworks in the composite films, which greatly reduces the interfacial thermal resistance between the matrix and fillers. Heat flow can be efficiently transferred along the continuous thermal conductive network, resulting in thermal conductivity improvement in the MXene/ANF composite films.[54−56] To further verify such improvement, the MA-20% and MA-80% were selected to be placed on the heating plate and heated from room temperature to 105 °C. The infrared thermal images show the surface temperature change of the composite films (Figure 5b). The surface temperature of MA-20% is 40.2 °C higher than MA-80% after heating for 120 s, indicating that the introduction of ANF can improve the heating transfer performance of the composite films (Figure 5c). Furthermore, due to great thermal conductivity, superior mechanical properties, and resistance to bending deformation, the MXene/ANF composite films have great potential as cooling installations for high-power flexible electronic devices. To demonstrate these applications, we selected the MA-20% and MA-80% for the heat dissipation of the LED chip. Figure 5d shows the flow diagram of the cooling devices of LED, where the films are used to act as thermal interface material (TIM) to connect the heat sink (Cu) and LED chip, and the LED operates at an applied voltage of 11 V. The changes in the central temperature of the LED chip loaded with different thermal interface materials were recorded by the infrared thermal imager, and the corresponding time-dependent temperature curves and infrared thermal images are shown in Figure 5e,f, respectively. The LED started to glow and generate a certain amount of heat after turning on the power. With the increase of the ANF content, the real-time central temperature of the LED chip gradually decreased, and MA-20% exhibited the best capacity for heat transmission. As shown in Figure 5f, the LED chip loaded with MA-20% presents the lowest temperature after working for 210 s and rapidly approached equilibrium temperature, indicative of a faster cooling rate.

Figure 6a shows the time-dependent temperature of the MXene/ANF composite films at the low direct voltages from 0.5 to 4 V. Due to the efficient conductive pathway, the surface temperature of the film increases continuously with the increase of the load voltage and reaches a steady-state temperature within 10 s. The infrared thermal images exhibit a uniform temperature distribution; the steady temperatures change from 31.6 at 0.5 V to 89.0 °C at 4 V (Figure 6d), indicating the high-efficiency electrothermal conversion capacity. According to the following equation

$$Q = \frac{U^2}{R}t$$

where Q, U, R, and t stand for the Joule heat, load voltage, resistance, and working time, respectively.[57] The steady-state temperatures of the film surface are linearly fitted to the square of the voltages (Figure 6b), which proves that the electrothermal conversion performance is consistent with the theoretically expected results. Figure 6c shows the cyclic tests of the electronic heating property. The surface temperature of the MXene/ANF composite film exhibits stable and periodic changes under different unloading and loading applied voltages, exhibiting its outstanding stability. The $I-V$ curve also shows the linear relationship between applied voltage and current, demonstrating the stable resistance of the composite film (Figure S20). Moreover, the MXene/ANF composite film exhibits long-term Joule heating performance for 3600 s at an applied voltage of 2.5 V, as shown in Figure 6e. The surface temperature was recorded at around 54.1 °C by infrared thermal images, and no temperature variation occurred, which certifies the durability for long-time working.

https://doi.org/10.1021/acsami.2c20101
ACS Appl. Mater. Interfaces 2023, 15, 4516−4526

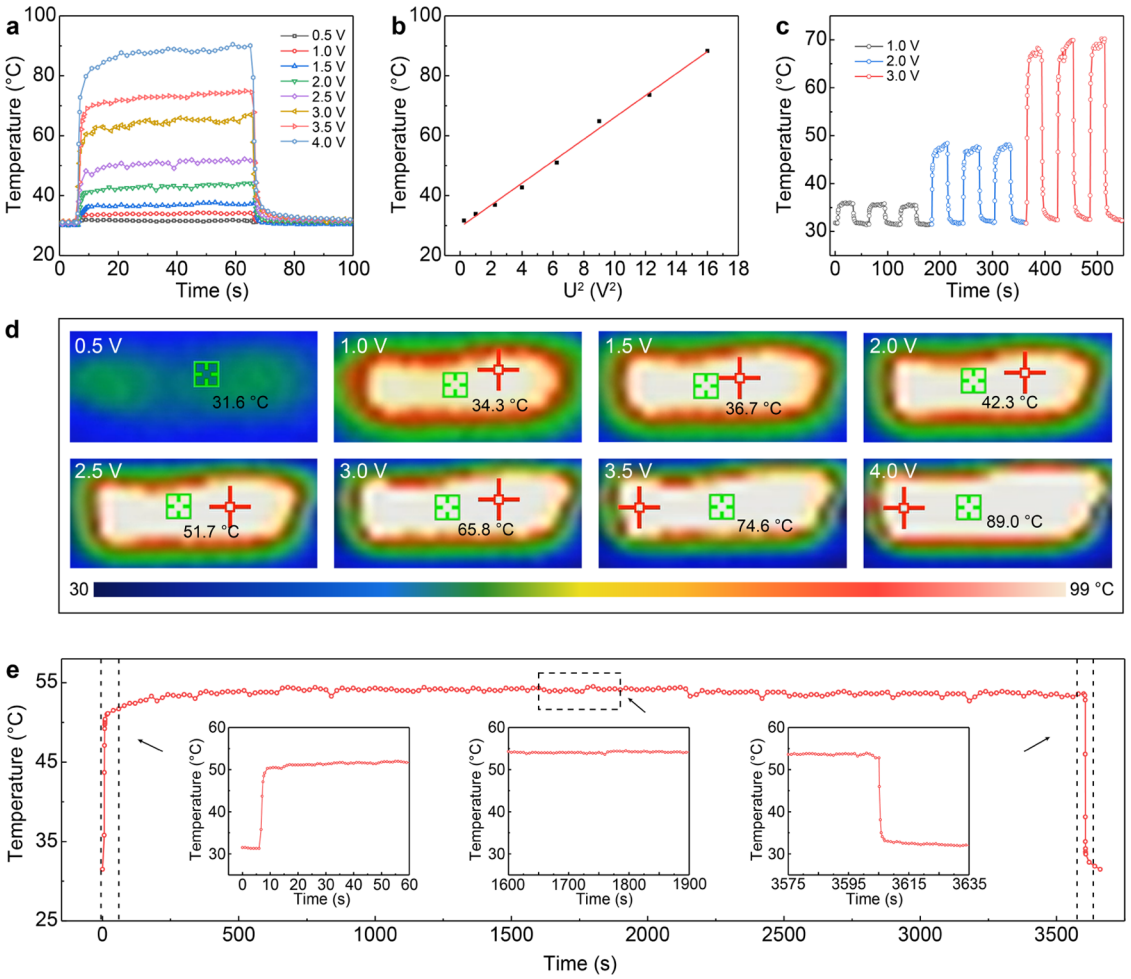

Figure 6. (a) Time-dependent temperature curves of the MXene/ANF film with 50 wt % MXene content under different applied voltages. (b) The test data and linear fitting of saturation temperature versus U^2. (c) The cyclic test of the MXene/ANF film at the applied voltages of 1.0, 2.0, and 3.0 V. (d) Infrared thermal images of the film at changed voltages. (e) Long-term temperature curve at an applied voltage of 2.5 V for 3600 s.

4. CONCLUSIONS

In summary, the MXene/ANF composite films were prepared through intermittent filtration and applied with excellent EMI shielding and heat dissipation. The MXene nanosheets have been oriented to form highly ordered "brick−mortar" structure and conductive networks, which enable great electrical conductivity, thermal conductivity, and mechanical strength. The resulting MXene/ANF with an MXene content of 50 wt % exhibits an excellent conductivity of 624.6 S/cm, an EMI shielding efficiency of 44.0 dB, and an SSE/t of 18 847.6 dB·cm^2/g. The hydrogen bonding of MXene and 1D rigid ANF endow the composite films with a superior tensile strength of 230.5 MPa, an elongation at break of 6.2%, and an outstanding toughness of 11.8 MJ/m^3. In addition, ANF enhances the through-plane thermal conductivity of the composite film up to 0.43 W/m·K, which is higher than pure MXene. The multifunctional MXene/ANF composite films reveal great potential in the areas of electronic communication, military, aerospace, microelectronics, and smart wearable electronics.

■ ASSOCIATED CONTENT

Supporting Information

The Supporting Information is available free of charge at https://pubs.acs.org/doi/10.1021/acsami.2c20101.

SEM of MAX; TEM and SAED images of MXene; optical and SEM images of PPTA fibers; Tyndall effect of ANF, MXene and MXene/ANF dispersion; schematic illustration of the preparation process; EDS mapping; electrical conductivity; SEM images of MXene/ANF films; XPS spectra; stress−strain curves; SEM images of the fracture surface; mechanical properties; contact angle; EMI shielding performance; schematic illustration of the EMI shielding mechanism; I−V curve of films; EMI shielding properties of MXene/ANF with different contents; mechanical properties of MXene/ANF with different contents and comparison of the EMI shielding performance of other materials (PDF)

■ AUTHOR INFORMATION

Corresponding Author

Bao-Wen Li − *State Key Laboratory of Advanced Technology for Materials Synthesis and Processing, Center of Smart Materials and Devices, Wuhan University of Technology, Wuhan 430070, China;* orcid.org/0000-0003-0846-6916; Email: bwli@whut.edu.cn

Authors

Chenxu Liu − *State Key Laboratory of Advanced Technology for Materials Synthesis and Processing, Center of Smart*

Materials and Devices, Wuhan University of Technology, Wuhan 430070, China

Yanan Ma − *State Key Laboratory of Advanced Technology for Materials Synthesis and Processing, Center of Smart Materials and Devices, Wuhan University of Technology, Wuhan 430070, China*

Yimei Xie − *State Key Laboratory of Advanced Technology for Materials Synthesis and Processing, Center of Smart Materials and Devices, Wuhan University of Technology, Wuhan 430070, China*

Junjie Zou − *State Key Laboratory of Advanced Technology for Materials Synthesis and Processing, Center of Smart Materials and Devices, Wuhan University of Technology, Wuhan 430070, China*

Han Wu − *State Key Laboratory of Advanced Technology for Materials Synthesis and Processing, Center of Smart Materials and Devices, Wuhan University of Technology, Wuhan 430070, China*

Shaohui Peng − *State Key Laboratory of Advanced Technology for Materials Synthesis and Processing, Center of Smart Materials and Devices, Wuhan University of Technology, Wuhan 430070, China*

Wei Qian − *Hubei Engineering Research Center of RF-Microwave Technology and Application, Wuhan University of Technology, Wuhan 430070, China*

Daping He − *Hubei Engineering Research Center of RF-Microwave Technology and Application, Wuhan University of Technology, Wuhan 430070, China;* orcid.org/0000-0002-0284-4990

Xin Zhang − *State Key Laboratory of Advanced Technology for Materials Synthesis and Processing, Center of Smart Materials and Devices, Wuhan University of Technology, Wuhan 430070, China;* orcid.org/0000-0003-4310-4187

Ce-Wen Nan − *State Key Laboratory of New Ceramics and Fine Processing, School of Materials Science and Engineering, Tsinghua University, Beijing 100084, China*

Complete contact information is available at: https://pubs.acs.org/10.1021/acsami.2c20101

Notes

The authors declare no competing financial interest.

■ ACKNOWLEDGMENTS

This work was supported by the National Key Research and Development Program of China (2020YFA0715000), the National Natural Science Foundation of China (Grant Nos. 52172124 and 51872214), the Fundamental Research Funds for the Central Universities (WUT: 2021III019JC, 2018III041GX), and China Postdoctoral Science Foundation (Grant No. 2022M712483).

■ REFERENCES

(1) Chen, J.; Huang, X.; Sun, B.; Jiang, P. Highly Thermally Conductive Yet Electrically Insulating Polymer/Boron Nitride Nanosheets Nanocomposite Films for Improved Thermal Management Capability. *ACS Nano* **2019**, *13*, 337−345.

(2) Weng, G.-M.; Li, J.; Alhabeb, M.; Karpovich, C.; Wang, H.; Lipton, J.; Maleski, K.; Kong, J.; Shaulsky, E.; Elimelech, M.; Gogotsi, Y.; Taylor, A. D. Layer-by-Layer Assembly of Cross-Functional Semi-Transparent MXene-Carbon Nanotubes Composite Films for Next-Generation Electromagnetic Interference Shielding. *Adv. Funct. Mater.* **2018**, *28*, No. 1803360.

(3) Yan, D.-X.; Pang, H.; Li, B.; Vajtai, R.; Xu, L.; Ren, P.-G.; Wang, J.-H.; Li, Z.-M. Structured Reduced Graphene Oxide/Polymer Composites for Ultra-Efficient Electromagnetic Interference Shielding. *Adv. Funct. Mater.* **2015**, *25*, 559−566.

(4) Agnihotri, N.; Chakrabarti, K.; De, A. Highly Efficient Electromagnetic Interference Shielding Using Graphite Nanoplatelet/Poly(3,4-Ethylenedioxythiophene)−Poly(Styrenesulfonate) Composites with Enhanced Thermal Conductivity. *RSC Adv.* **2015**, *5*, 43765−43771.

(5) Wu, Y.; Wang, Z.; Liu, X.; Shen, X.; Zheng, Q.; Xue, Q.; Kim, J.-K. Ultralight Graphene Foam/Conductive Polymer Composites for Exceptional Electromagnetic Interference Shielding. *ACS Appl. Mater. Interfaces* **2017**, *9*, 9059−9069.

(6) Chen, Z.; Xu, C.; Ma, C.; Ren, W.; Cheng, H.-M. Lightweight and Flexible Graphene Foam Composites for High-Performance Electromagnetic Interference Shielding. *Adv. Mater.* **2013**, *25*, 1296−1300.

(7) Yousefi, N.; Sun, X.; Lin, X.; Shen, X.; Jia, J.; Zhang, B.; Tang, B.; Chan, M.; Kim, J.-K. Highly Aligned Graphene/Polymer Nanocomposites with Excellent Dielectric Properties for High-Performance Electromagnetic Interference Shielding. *Adv. Mater.* **2014**, *26*, 5480−5487.

(8) Li, Y.; Pei, X.; Shen, B.; Zhai, W.; Zhang, L.; Zheng, W. Polyimide/Graphene Composite Foam Sheets with Ultrahigh Thermostability for Electromagnetic Interference Shielding. *RSC Adv.* **2015**, *5*, 24342−24351.

(9) Yan, D.-X.; Ren, P.-G.; Pang, H.; Fu, Q.; Yang, M.-B.; Li, Z.-M. Efficient Electromagnetic Interference Shielding of Lightweight Graphene/Polystyrene Composite. *J. Mater. Chem.* **2012**, *22*, 18772−18774.

(10) Zeng, Z.; Chen, M.; Jin, H.; Li, W.; Xue, X.; Zhou, L.; Pei, Y.; Zhang, H.; Zhang, Z. Thin and Flexible Multi-Walled Carbon Nanotube/Waterborne Polyurethane Composites with High-Performance Electromagnetic Interference Shielding. *Carbon* **2016**, *96*, 768−777.

(11) Zhang, H.; Sun, X.; Heng, Z.; Chen, Y.; Zou, H.; Liang, M. Robust and Flexible Cellulose Nanofiber/Multiwalled Carbon Nanotube Film for High-Performance Electromagnetic Interference Shielding. *Ind. Eng. Chem. Res.* **2018**, *57*, 17152−17160.

(12) Hu, P.; Lyu, J.; Fu, C.; Gong, W.; Liao, J.; Lu, W.; Chen, Y.; Zhang, X. Multifunctional Aramid Nanofiber/Carbon Nanotube Hybrid Aerogel Films. *ACS Nano* **2020**, *14*, 688−697.

(13) Huang, J.; Li, J.; Xu, X.; Hua, L.; Lu, Z. In Situ Loading of Polypyrrole onto Aramid Nanofiber and Carbon Nanotube Aerogel Fibers as Physiology and Motion Sensors. *ACS Nano* **2022**, *16*, 8161−8171.

(14) Zhang, H.; Zhang, G.; Gao, Q.; Tang, M.; Ma, Z.; Qin, J.; Wang, M.; Kim, J.-K. Multifunctional Microcellular PVDF/Ni-Chains Composite Foams with Enhanced Electromagnetic Interference Shielding and Superior Thermal Insulation Performance. *Chem. Eng. J.* **2020**, *379*, No. 122304.

(15) Wu, L.; Wang, L.; Guo, Z.; Luo, J.; Xue, H.; Gao, J. Durable and Multifunctional Superhydrophobic Coatings with Excellent Joule Heating and Electromagnetic Interference Shielding Performance for Flexible Sensing Electronics. *ACS Appl. Mater. Interfaces* **2019**, *11*, 34338−34347.

(16) Lee, T.-W.; Lee, S.-E.; Jeong, Y. G. Highly Effective Electromagnetic Interference Shielding Materials Based on Silver Nanowire/Cellulose Papers. *ACS Appl. Mater. Interfaces* **2016**, *8*, 13123−13132.

(17) Shui, X.; Chung, D. D. L. Nickel Filament Polymer-Matrix Composites with Low Surface Impedance and High Electromagnetic Interference Shielding Effectiveness. *J. Electron. Mater.* **1997**, *26*, 928−934.

(18) Xing, D.; Lu, L.; Teh, K. S.; Wan, Z.; Xie, Y.; Tang, Y. Highly Flexible and Ultra-Thin Ni-Plated Carbon-Fabric/Polycarbonate Film for Enhanced Electromagnetic Interference Shielding. *Carbon* **2018**, *132*, 32−41.

(19) Subramaniam, C.; Yasuda, Y.; Takeya, S.; Ata, S.; Nishizawa, A.; Futaba, D.; Yamada, T.; Hata, K. Carbon Nanotube-Copper Exhibiting Metal-like Thermal Conductivity and Silicon-like Thermal Expansion for Efficient Cooling of Electronics. *Nanoscale* **2014**, *6*, 2669−2674.
(20) Ma, J.; Wang, K.; Zhan, M. A Comparative Study of Structure and Electromagnetic Interference Shielding Performance for Silver Nanostructure Hybrid Polyimide Foams. *RSC Adv.* **2015**, *5*, 65283−65296.
(21) Xu, Y.; Kraemer, D.; Song, B.; Jiang, Z.; Zhou, J.; Loomis, J.; Wang, J.; Li, M.; Ghasemi, H.; Huang, X.; Li, X.; Chen, G. Nanostructured Polymer Films with Metal-like Thermal Conductivity. *Nat. Commun.* **2019**, *10*, No. 1771.
(22) Wan, S.; Li, Y.; Mu, J.; Aliev, A. E.; Fang, S.; Kotov, N. A.; Jiang, L.; Cheng, Q.; Baughman, R. H. Sequentially Bridged Graphene Sheets with High Strength, Toughness, and Electrical Conductivity. *Proc. Natl. Acad. Sci. U.S.A.* **2018**, *115*, 5359−5364.
(23) Wu, K.; Wang, J.; Liu, D.; Lei, C.; Liu, D.; Lei, W.; Fu, Q. Highly Thermoconductive, Thermostable, and Super-Flexible Film by Engineering 1D Rigid Rod-Like Aramid Nanofiber/2D Boron Nitride Nanosheets. *Adv. Mater.* **2020**, *32*, No. 1906939.
(24) Zhou, B.; Zhang, Z.; Li, Y.; Han, G.; Feng, Y.; Wang, B.; Zhang, D.; Ma, J.; Liu, C. Flexible, Robust, and Multifunctional Electromagnetic Interference Shielding Film with Alternating Cellulose Nanofiber and MXene Layers. *ACS Appl. Mater. Interfaces* **2020**, *12*, 4895−4905.
(25) Iqbal, A.; Sambyal, P.; Koo, C. M. 2D MXenes for Electromagnetic Shielding: A Review. *Adv. Funct. Mater.* **2020**, *30*, No. 2000883.
(26) Ma, Y.; Liu, N.; Li, L.; Hu, X.; Zou, Z.; Wang, J.; Luo, S.; Gao, Y. A Highly Flexible and Sensitive Piezoresistive Sensor Based on MXene with Greatly Changed Interlayer Distances. *Nat. Commun.* **2017**, *8*, No. 1207.
(27) Han, M.; Shuck, C. E.; Rakhmanov, R.; Parchment, D.; Anasori, B.; Koo, C. M.; Friedman, G.; Gogotsi, Y. Beyond $Ti_3C_2T_x$: MXenes for Electromagnetic Interference Shielding. *ACS Nano* **2020**, *14*, 5008−5016.
(28) Tian, W.; VahidMohammadi, A.; Reid, M. S.; Wang, Z.; Ouyang, L.; Erlandsson, J.; Pettersson, T.; Wågberg, L.; Beidaghi, M.; Hamedi, M. M. Multifunctional Nanocomposites with High Strength and Capacitance Using 2D MXene and 1D Nanocellulose. *Adv. Mater.* **2019**, *31*, No. 1902977.
(29) Wang, Y.; Yue, Y.; Cheng, F.; Cheng, Y.; Ge, B.; Liu, N.; Gao, Y. $Ti_3C_2T_x$ MXene-Based Flexible Piezoresistive Physical Sensors. *ACS Nano* **2022**, *16*, 1734−1758.
(30) Ma, Y.; Cheng, Y.; Wang, J.; Fu, S.; Zhou, M.; Yang, Y.; Li, B.; Zhang, X.; Nan, C.-W. Flexible and Highly-Sensitive Pressure Sensor Based on Controllably Oxidized MXene. *InfoMat* **2022**, *4* (9), No. e12328.
(31) Ma, Y.; Yue, Y.; Zhang, H.; Cheng, F.; Zhao, W.; Rao, J.; Luo, S.; Wang, J.; Jiang, X.; Liu, Z.; Liu, N.; Gao, Y. 3D Synergistical MXene/Reduced Graphene Oxide Aerogel for a Piezoresistive Sensor. *ACS Nano* **2018**, *12*, 3209−3216.
(32) Shahzad, F.; Alhabeb, M.; Hatter, C. B.; Anasori, B.; Man Hong, S.; Koo, C. M.; Gogotsi, Y. Electromagnetic Interference Shielding with 2D Transition Metal Carbides (MXenes). *Science* **2016**, *353*, 1137−1140.
(33) Wan, S.; Fang, S.; Jiang, L.; Cheng, Q.; Baughman, R. H. Strong, Conductive, Foldable Graphene Sheets by Sequential Ionic and π Bridging. *Adv. Mater.* **2018**, *30*, No. 1802733.
(34) Cao, W.-T.; Chen, F.-F.; Zhu, Y.-J.; Zhang, Y.-G.; Jiang, Y.-Y.; Ma, M.-G.; Chen, F. Binary Strengthening and Toughening of MXene/Cellulose Nanofiber Composite Paper with Nacre-Inspired Structure and Superior Electromagnetic Interference Shielding Properties. *ACS Nano* **2018**, *12*, 4583−4593.
(35) Ma, Z.; Kang, S.; Ma, J.; Shao, L.; Zhang, Y.; Liu, C.; Wei, A.; Xiang, X.; Wei, L.; Gu, J. Ultraflexible and Mechanically Strong Double-Layered Aramid Nanofiber−$Ti_3C_2T_x$ MXene/Silver Nanowire Nanocomposite Papers for High-Performance Electromagnetic Interference Shielding. *ACS Nano* **2020**, *14*, 8368−8382.
(36) Yang, B.; Wang, L.; Zhang, M.; Luo, J.; Ding, X. Timesaving, High-Efficiency Approaches To Fabricate Aramid Nanofibers. *ACS Nano* **2019**, *13*, 7886−7897.
(37) Yang, B.; Wang, L.; Zhang, M.; Luo, J.; Lu, Z.; Ding, X. Fabrication, Applications, and Prospects of Aramid Nanofiber. *Adv. Funct. Mater.* **2020**, *30*, No. 2000186.
(38) Wang, L.; Zhang, M.; Yang, B.; Ding, X.; Tan, J.; Song, S.; Nie, J. Flexible, Robust, and Durable Aramid Fiber/CNT Composite Paper as a Multifunctional Sensor for Wearable Applications. *ACS Appl. Mater. Interfaces* **2021**, *13*, 5486−5497.
(39) Lin, J.; Bang, S. H.; Malakooti, M. H.; Sodano, H. A. Isolation of Aramid Nanofibers for High Strength and Toughness Polymer Nanocomposites. *ACS Appl. Mater. Interfaces* **2017**, *9*, 11167−11175.
(40) Hu, D.; Wang, S.; Zhang, C.; Yi, P.; Jiang, P.; Huang, X. Ultrathin MXene-Aramid Nanofiber Electromagnetic Interference Shielding Films with Tactile Sensing Ability Withstanding Harsh Temperatures. *Nano Res.* **2021**, *14*, 2837−2845.
(41) Wang, J.; Ma, X.; Zhou, J.; Du, F.; Teng, C. Bioinspired, High-Strength, and Flexible MXene/Aramid Fiber for Electromagnetic Interference Shielding Papers with Joule Heating Performance. *ACS Nano* **2022**, *16*, 6700−6711.
(42) Wong, M.; Ishige, R.; White, K. L.; Li, P.; Kim, D.; Krishnamoorti, R.; Gunther, R.; Higuchi, T.; Jinnai, H.; Takahara, A.; Nishimura, R.; Sue, H.-J. Large-Scale Self-Assembled Zirconium Phosphate Smectic Layers via a Simple Spray-Coating Process. *Nat. Commun.* **2014**, *5*, No. 3589.
(43) Guo, F.; Shen, X.; Zhou, J.; Liu, D.; Zheng, Q.; Yang, J.; Jia, B.; Lau, A. K. T.; Kim, J.-K. Highly Thermally Conductive Dielectric Nanocomposites with Synergistic Alignments of Graphene and Boron Nitride Nanosheets. *Adv. Funct. Mater.* **2020**, *30*, No. 1910826.
(44) Wan, S.; Li, X.; Chen, Y.; Liu, N.; Du, Y.; Dou, S.; Jiang, L.; Cheng, Q. High-Strength Scalable MXene Films through Bridging-Induced Densification. *Science* **2021**, *374*, 96−99.
(45) Lei, C.; Zhang, Y.; Liu, D.; Wu, K.; Fu, Q. Metal-Level Robust, Folding Endurance, and Highly Temperature-Stable MXene-Based Film with Engineered Aramid Nanofiber for Extreme-Condition Electromagnetic Interference Shielding Applications. *ACS Appl. Mater. Interfaces* **2020**, *12*, 26485−26495.
(46) Yang, B.; Li, W.; Zhang, M.; Wang, L.; Ding, X. Recycling of High-Value-Added Aramid Nanofibers from Waste Aramid Resources via a Feasible and Cost-Effective Approach. *ACS Nano* **2021**, *15*, 7195−7207.
(47) Naguib, M.; Kurtoglu, M.; Presser, V.; Lu, J.; Niu, J.; Heon, M.; Hultman, L.; Gogotsi, Y.; Barsoum, M. W. Two-Dimensional Nanocrystals Produced by Exfoliation of Ti_3AlC_2. *Adv. Mater.* **2011**, *23*, 4248−4253.
(48) Ghidiu, M.; Lukatskaya, M. R.; Zhao, M.-Q.; Gogotsi, Y.; Barsoum, M. W. Conductive Two-Dimensional Titanium Carbide 'Clay' with High Volumetric Capacitance. *Nature* **2014**, *516*, 78−81.
(49) Yang, M.; Cao, K.; Sui, L.; Qi, Y.; Zhu, J.; Waas, A.; Arruda, E. M.; Kieffer, J.; Thouless, M. D.; Kotov, N. A. Dispersions of Aramid Nanofibers: A New Nanoscale Building Block. *ACS Nano* **2011**, *5*, 6945−6954.
(50) Cao, W.; Ma, C.; Tan, S.; Ma, M.; Wan, P.; Chen, F. Ultrathin and Flexible CNTs/MXene/Cellulose Nanofibrils Composite Paper for Electromagnetic Interference Shielding. *Nano-Micro Lett.* **2019**, *11*, 72.
(51) Liu, L.-X.; Chen, W.; Zhang, H.-B.; Ye, L.; Wang, Z.; Zhang, Y.; Min, P.; Yu, Z.-Z. Super-Tough and Environmentally Stable Aramid Nanofiber@MXene Coaxial Fibers with Outstanding Electromagnetic Interference Shielding Efficiency. *Nano-Micro Lett.* **2022**, *14*, 111.
(52) Wan, Y.-J.; Wang, X.-Y.; Li, X.-M.; Liao, S.-Y.; Lin, Z.-Q.; Hu, Y.-G.; Zhao, T.; Zeng, X.-L.; Li, C.-H.; Yu, S.-H.; Zhu, P.-L.; Sun, R.; Wong, C.-P. Ultrathin Densified Carbon Nanotube Film with "Metal-like" Conductivity, Superior Mechanical Strength, and Ultrahigh Electromagnetic Interference Shielding Effectiveness. *ACS Nano* **2020**, *14*, 14134−14145.

https://doi.org/10.1021/acsami.2c20101
ACS Appl. Mater. Interfaces 2023, 15, 4516−4526

(53) Zhang, J.; Kong, N.; Uzun, S.; Levitt, A.; Seyedin, S.; Lynch, P. A.; Qin, S.; Han, M.; Yang, W.; Liu, J.; Wang, X.; Gogotsi, Y.; Razal, J. M. Scalable Manufacturing of Free-Standing, Strong $Ti_3C_2T_x$ MXene Films with Outstanding Conductivity. *Adv. Mater.* **2020**, *32*, No. 2001093.
(54) Wang, Y.; Xu, N.; Li, D.; Zhu, J. Thermal Properties of Two Dimensional Layered Materials. *Adv. Funct. Mater.* **2017**, *27*, No. 1604134.
(55) Guerra, V.; Wan, C.; McNally, T. Thermal Conductivity of 2D Nano-Structured Boron Nitride (BN) and Its Composites with Polymers. *Prog. Mater. Sci.* **2019**, *100*, 170−186.
(56) Burger, N.; Laachachi, A.; Ferriol, M.; Lutz, M.; Toniazzo, V.; Ruch, D. Review of Thermal Conductivity in Composites: Mechanisms, Parameters and Theory. *Prog. Polym. Sci.* **2016**, *61*, 1−28.
(57) Wu, H.; Xie, Y.; Ma, Y.; Zhang, B.; Xia, B.; Zhang, P.; Qian, W.; He, D.; Zhang, X.; Li, B.-W.; Nan, C.-W. Aqueous MXene/Xanthan Gum Hybrid Inks for Screen-Printing Electromagnetic Shielding, Joule Heater, and Piezoresistive Sensor. *Small* **2022**, *18*, No. 2107087.

https://doi.org/10.1021/acsami.2c20101
ACS Appl. Mater. Interfaces 2023, 15, 4516−4526